agronomy

MDPI

Article

Machine Learning Approach to Predict Flow Regime Index of a Stellate Water-Retaining Labyrinth Channel Emitter

Yanfei Li [1,2], Xianying Feng [1,2,*], Xingchang Han [1,2,3], Yitian Sun [1,2,3] and Hui Li [1,2]

1 School of Mechanical Engineering, Shandong University, Shandong 250061, China
2 Key Laboratory of High Efficiency and Clean Mechanical Manufacture of Ministry of Education, Shandong University, Shandong 250061, China
3 Shandong Academy of Agricultural Machinery Sciences, Shandong 250100, China
* Correspondence: fxying@sdu.edu.cn

Abstract: Accurate calculation of the flow regime index in the design and development stage of a drip irrigation emitter plays an essential role. In this study, machine learning technologies were used to establish the relationship between flow channel structural parameters of the novel stellate water-retaining labyrinth channel (SWRLC) irrigation emitter and its flow regime index. The training dataset and test dataset were built by computational fluid dynamics (CFD) simulation and experimental study. The extreme learning machine (ELM), backpropagation neural network (BPNN), and traditional multiple linear regression (MLR) models were developed for the prediction of the flow regime index of the SWRLC emitter. The input parameters matrix consisted of the length of the trapezoid baseline, angle between the hypotenuses of adjacent trapezoids, trapezoid height, radius of stellate water-retaining structure, spacing of two symmetric trapezoids, path depth, and SWRLC unit number, while flow regime index x was the output of the models. The comprehensive indicator (CI) was proposed, and root mean square error (RMSE), mean absolute error (MAE), mean bias error value (MBE), and coefficient of determination (R^2) were used to introduce the reliable assessment of the three models. The comparison results showed that the ELM model had the lowest errors, with the CI, RMSE, MAE, and R^2 were 1.96×10^{-11}, 0.00163, 0.00126, and 91.49%, respectively. The BPNN model had the lowest MBE error with the value of 1.03×10^{-4}. The ELM and BPNN models were available and had acceptable accuracy for predicting the flow regime index of the emitter, saving both time and cost and increasing efficiency in the design and development stage. According to the CI, the ELM model performed best, followed by the BPNN model with a minor discrepancy.

Keywords: drip irrigation; flow regime index; computational fluid dynamics; extreme learning machine

check for updates

Citation: Li, Y.; Feng, X.; Han, X.; Sun, Y.; Li, H. Machine Learning Approach to Predict Flow Regime Index of a Stellate Water-Retaining Labyrinth Channel Emitter. *Agronomy* **2023**, *13*, 1063. https://doi.org/10.3390/agronomy13041063

Academic Editor: Jose Manuel Gonçalves

Received: 6 March 2023
Revised: 30 March 2023
Accepted: 3 April 2023
Published: 6 April 2023

1. Introduction

Rational conservation and full utilization of water resources is an important measure to improve agricultural yield. Drip irrigation is one of the most water-saving irrigation technologies for farmland irrigation, which has several advantages over other watering methods, such as water consumption reduction, improving fertilizer and nutrients in plant roots, and increasing production and quality [1]. The drip irrigation emitter is the key component of a drip irrigation system, which reflects the uniformity of irrigation [2]. In other words, the performance of a drip irrigation system largely depends on the discharge uniformity of a drip irrigation emitter. The success of discharge uniformity of a drip irrigation emitter relays on its hydraulic properties [3]. The flow regime index is a crucial index to measure the hydraulic properties of an emitter, and its values (between 0 and 1) provide the superiority level of the hydraulic performance [4].

The smaller the flow regime index, the less sensitive the discharge of the emitter is to working pressure [5]. The flow regime in the emitter flow channel is divided into three categories of laminar flow (flow regime index is 1), turbulent flow (flow regime index is 0.3–0.8), and absolute pressure compensation (flow regime index is 0) based on flow regime index values. The regime flow in the labyrinth emitter flow channel is turbulent flow [6]. The flow regime index is one of the indicators to be considered in the design and development stage of the labyrinth channel emitter. Different flow channel units of emitters have different flow regime index values [7]. Even if the same flow channel shape is the same, different flow channel structure parameters lead to considerable differences in flow regime index. Therefore, it is very important to establish the relationship between key flow channel structural parameters of the emitter and its flow regime index accurately and quickly in the stage of design development and optimization.

In recent decades, CFD has been widely used in the design and optimization stage of labyrinth emitters because it saves development cycle time and economic cost. Feng et al. [8] used CFD simulation and digital particle image velocimetry (DPIV) methods to study the hydraulic performance of tooth labyrinth channel emitters, and the results showed that the flow regime index errors of LES model and RNG $k-\varepsilon$ model were relatively smaller. Xu et al. [9] obtained the smaller flow regime index error (about 0.6%) for a pit drip irrigation emitter by CFD simulation combined with a hydraulic performance test. Guo et al. [10] analyzed the errors of three kinds of wall function and seven classes physical models and showed that the numerical simulation accuracy of the enhanced wall function was better and the calculation accuracy of RNG $k-\varepsilon$ model was best, taking the macroscopic flow rate index as the evaluation standard. Xing et al. [11] applied physical experiments and CFD simulation calculations to improve the hydraulic performance of perforated drip irrigation emitters and found that the calculation method of the CFD software package was reliable. Although many researchers have achieved good results with the use of CFD to simulate the hydraulic performance and flow regime index of labyrinth channel emitters, the relationship between the key structural parameters of a flow channel and its flow regime index cannot be directly established.

At present, a single-factor test method, multi-factor orthogonal test method, and regression model are used to research the relationship between structural parameters and the flow regime index by many scholars. Ai-Alamoud et al. [12] found that trapezoidal unit (dentations) numbers and height variables had the most significant influence on hydraulic performance compared with other parameter variables. Yu et al. [13] indicated that the flow regime index declined with the decrease in dentation angle of the tooth labyrinth channel by the single-factor test method combined with CFD simulation. Zhang Zhong et al. [14] showed that the flow regime indices of 13 fractal flow paths were around 0.49 and the flow coefficient had a significantly positive relationship with flow path width and depth, while a highly significant negative correlation with flow path length was observed. Zhang et al. [15] showed that the turning angle of tooth was the most important factor affecting pressure loss coefficient followed by the width of tooth top and tooth height using an orthogonal design method combined with a multivariable regression method. Only the independent influence of each structural parameter of a labyrinth irrigation emitter on its hydraulic performance or flow regime index are discussed, and interaction between parameters is not considered in many studies. The relationship between the structural parameter of a labyrinth irrigation emitter on its hydraulic performance or flow regime index has also not been determined directly.

Recently, with the rapid development of computer technology, machine learning technologies have been developed as helpful methods to solve nonlinear, uncertain, multivariable, and complicated issues. The models, e.g., backpropagation neural network (BPNN) and extreme learning machine (ELM), established by machine learning technologies have been widely applied in various fields, such as health monitoring [16], wind speed prediction [17], signal processing [18], flume discharge estimation [19], agricultural robotics [20], detection and classification of plant leaf diseases [21], fruit quality identification [22], fruit detection and counting [23], soil moisture prediction [24], modelling and forecasting reservoir sedimentation of irrigation dams [25], irrigation decisions for tomato seedlings [26], saturated hydraulic conductivity estimation [27], computing of the crop water stress index [28], and irrigation water allocation optimization [29]. In terms of wisdom irrigation systems, machine learning techniques are used to predict the hydraulic performance of drip irrigation emitters by many researchers. Mattar and Alamoud [30] developed an artificial neural network (ANN) model and multiple linear regression (MLR) model to estimate the hydraulic performance of labyrinth channel emitters and found that the relatively low errors obtained by the ANN approach led to high model predictability. Lavanhoil et al. [31] employed nonlinear regression and an ANN model to predict pressure–discharge curves of trapezoidal labyrinth channels and revealed that both models were accurate and enabled rapid prediction of the emitter's discharge. Mattar et al. [32] exploited gene expression programming (GEP) to model and predict flow variation and manufacturer's coefficient of variation of different labyrinth channel emitters and discovered that the performance of the developed GEP models was better at predicting flow variation and manufacturer's coefficient of variation for non-pressure-compensating emitters than pressure-compensating ones. Seyedzadeh et al. [33] applied five machine learning models to predict modified coefficient of drip tape irrigation and uncovered that the least square support vector machine (LS-SVM) model had the lowest error, followed by the neuro-fuzzy sub-clustering (NF-SC) model with a slight difference. Mattar et al. [34] used an ANN model and GEP model combined with experimental study to predict flow variation and manufacturer's coefficient of variation of labyrinth channel emitters, and confirmed that ANN models were superior to the GEP models for the prediction of the hydraulic performance of emitters.

Although the application of machine learning technologies in the prediction of hydraulic performance (discharge, modified coefficient, flow variation, and manufacturer's coefficient) of drip irrigation emitters had achieved good results, there is no literature to estimate the flow regime index during the design and development of drip irrigation emitters. A review of the literature by the scholars showed that there has also been no attempt to employ machine learning technologies to establish the relationship between flow channel structural parameters of an irrigation emitter and its flow regime index in the design and development stage. As we all know, since the determination of the flow channel structure parameters of the emitter means that the flow regime index of the emitter is determined, it is particularly important to determine its flow regime index in the design and development stage. Additionally, most scholars did not study the relationship between the structural parameters of the novel labyrinth drip irrigation emitter and its flow regime index, and instead examined the widely used tooth drip irrigation emitter. In this study, the ELM, BPNN, and MLR models were developed to build the relationship between the flow channel structural parameters of the SWRLC emitter and its flow regime index combined with CFD simulation and experimental study indices. The three models were evaluated in terms of their accuracy and precision for predicting the flow regime index of a SWRLC emitter in the design and development stage.

2. Materials and Methods

2.1. Geometric Design of Study

For increasing the diversity of flow channel cross-sectional structure types and the generation of head loss, a new type of stellate water-retaining labyrinth channel (SWRLC) structure was proposed and designed in this study. The SWRLC unit was composed of a stellate water-retaining structure and two symmetrical isosceles trapezoid structures without baselines [35]. The characteristics and parameters of the SWRLC unit are shown in Figure 1. The three-dimensional model of the SWRLC emitter is shown in Figure 2. Therefore, each emitter was characterized by its structural design in terms of the key parameters of length of the trapezoid baseline (s), angle between the hypotenuses of adjacent trapezoids (θ), trapezoid height (h), radius of stellate water-retaining structure (r), and spacing of two symmetric trapezoids (a), as well as path depth (d) and SWRLC unit number (n). Generally, the discharge of the emitter is required to be less than or equal to 12 L/h. The range of the crucial geometric parameters was selected in light of design requirements and discharge rules of emitters. The key design parameters of emitters are provided in Table 1.

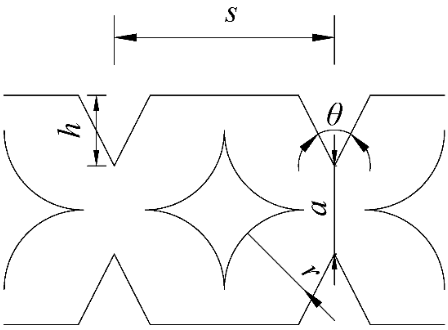

Figure 1. Schematic diagram of SWRLC unit structure.

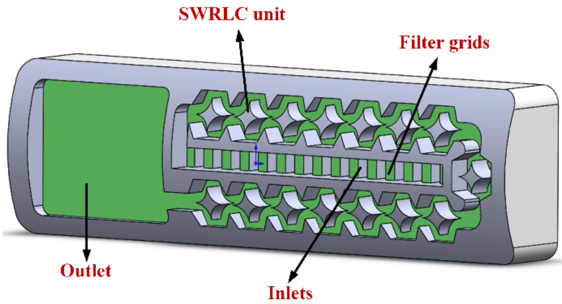

Figure 2. 3D physical model of SWRLC emitter.

Table 1. Key design parameters of SWRLC emitter.

s (mm)	*θ* (°)	*h* (mm)	*r* (mm)	*a* (mm)	*d* (mm)	*n*
2.10–2.50	20–60	0.60–1.00	0.60–1.00	0.45–0.60	0.90–1.30	10–19

2.2. Selection of Data

An increasing number of scholars employ numerical simulation methods to design and develop emitters [36–38]. For saving costs and shortening the development cycle, computational fluid dynamics (CFD) technology was applied for establishing the dataset. To obtain the simulated data, computational fluid dynamics (CFD) was used to simulate the internal flow field of the SWRLC emitter. Water flow in the SWRLC emitter was considered as a viscous incompressible fluid. The heat exchange of the SWRLC emitter could be ignored. Therefore, the two basic governing equations are as follows.

The continuity equation is as follows:

$$\mathrm{div}\ \boldsymbol{u} = 0 \tag{1}$$

The Navier–Stokes equations are as follows:

$$\frac{\partial(\rho u)}{\partial t} + \mathrm{div}(\rho u \boldsymbol{u}) = \mathrm{div}(\mu \cdot \mathrm{grad}\ u) - \frac{\partial p}{\partial x} \tag{2}$$

$$\frac{\partial(\rho v)}{\partial t} + \mathrm{div}(\rho v \boldsymbol{u}) = \mathrm{div}(\mu \cdot \mathrm{grad}\ v) - \frac{\partial p}{\partial y} \tag{3}$$

$$\frac{\partial(\rho w)}{\partial t} + \mathrm{div}(\rho w \boldsymbol{u}) = \mathrm{div}(\mu \cdot \mathrm{grad}\ w) - \frac{\partial p}{\partial z} \tag{4}$$

where $\boldsymbol{u}$ is velocity, ρ is the density, p represents pressure, μ is dynamic viscosity coefficient, u, v, and w are the components of the velocity vector $\boldsymbol{u}$ in the x, y, and z direction, respectively.

A total of 135 three-dimensional models of the SWRLC emitter with different geometric parameters were established using SolidWorks2018 software (Dassault Systemes, Waltham, MA, USA). The three-dimensional fluid domain models of the SWRLC emitter were established using SpaceClaim2021R1 software (ANSYS, Canonsburg, PA, USA). The grids were created using FluentMeshing2021R2 software (ANSYS, Canonsburg, PA, USA), and their qualities were examined. The skewness, based on the deviation from a normalized equilateral angle, was less than 0.5, which indicated that the mesh quality was acceptable. The realizable $k - \varepsilon$ model was chosen as the turbulence model. The wall function was set to standard. The volume meshes were filled by poly-hexcore-type mesh for the realizable $k - \varepsilon$ model. The meshes were constructed with $y^+ \leq 10$ for the realizable $k - \varepsilon$ model in order to refine more mesh close to the wall.

The independence of the meshing was performed to verify the reliability of the realizable $k - \varepsilon$ model simulation results. The velocities of point 1 (coordinates were $x = -4.54$ mm, $y = 2.35$ mm, $z = -0.75$ mm) and point 2 (coordinates were $x = -3.29$ mm, $y = 3.50$ mm, $z = -0.75$ mm) for different mesh elements are shown in Figure 3. The results of the mesh independence study showed that the change in velocity was minor when the mesh cell number was at least 2.51×10^6. It is considered that the influence of mesh can be ignored at this point. Therefore, the mesh cell numbers for the realizable $k - \varepsilon$ model were selected as 2.51×10^6. In that way, the accuracy of simulation result was not dependent on meshing.

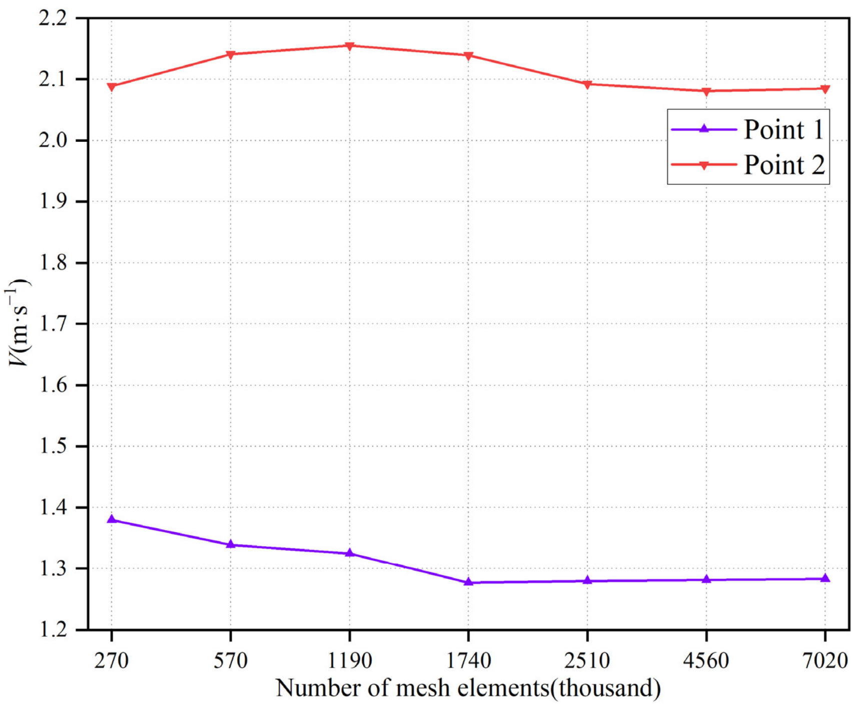

Figure 3. The results of the mesh independence study for the realizable $k - \varepsilon$ model.

For the flow field calculation of the SWRLC emitter flow channel, the boundary condition of inlet was set to the pressure inlet that was set as 20 kPa, 60 kPa, 100 kPa, 140 kPa, and 180 kPa, respectively. The settings of the other simulation parameters were the same as those of Li et al. [35].

Empirically, the flow regime index might be obtained from the relationship between emitter discharge and operating pressure as follows:

$$q = kP^x \tag{5}$$

where q represents the emitter discharge, k is the discharge coefficient, x is the flow regime index, and P is the operating pressure.

2.3. Backpropagation Neural Network (BPNN)

A BPNN is a feedforward neural network, which is characterized by signal forward transmission and error backpropagation. Its topological structure is shown in Figure 4. Here, $x_{1,2,\ldots,n}$, $y_{1,2,\ldots,n}$, and w_{ij} β_{jk} are input values, predicted values, and weights of BPNN, respectively. As can be seen from the figure, BPNN can be regarded as a nonlinear function, and the input value and predicted value of the network are the independent and dependent variables of the function, respectively.

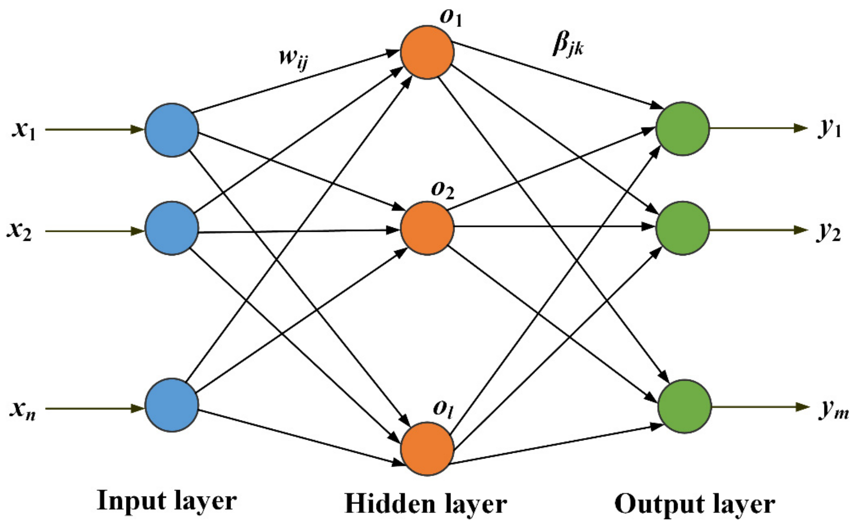

Figure 4. The topological structure of BPNN.

The training process enables BPNN to gain memory and prediction, which includes the following steps:

1. Initialization. Weights between the input layer and hidden layer (w_{ij}), weights between the hidden layer and output layer (β_{jk}), thresholds of the hidden layer (b), thresholds of the output layer (c), and learning rate (η) are initialized, and activation function (f ()) is selected.

2. Hidden layer output. The hidden layer output (H) can be represented as follows:

$$H_j = f(\sum_{i=1}^{n} w_{ij}x_i - b_j) \tag{6}$$

where $j = 1, 2, \ldots, l$, l, and f are the number of nodes and activation function in hidden layer, respectively.

3. Output layer output. The output layer output (O) can be expressed as follows:

$$O_k = \sum_{j=1}^{l} H_j\beta_{jk} - c_k \tag{7}$$

where $k = 1, 2, \ldots, m$ and m is the number of nodes in output layer.

4. Error calculation. The predicted error of BPNN can be given as follows:

$$e_k = Y_k - O_k \tag{8}$$

where Y_k is the desired output.

5. Updating weights. Updated weights between the input layer and hidden layer (w_{ij}) and updated weights between the hidden layer and output layer (β_{jk}) might be obtained as follows:

$$w_{ij} = w_{ij} + \eta H_j(1 - H_j)x(i)\sum_{k=1}^{m} \beta_{ik} e_k \tag{9}$$

$$\beta_{jk} = \beta_{jk} + \eta H_j e_k \tag{10}$$

6. Updating thresholds. The updated thresholds of the hidden layer (b_j) and updated thresholds of the output layer (c_k) might be obtained as follows:

$$b_j = b_j + \eta H_j(1 - H_j)\sum_{k=1}^{m} \beta_{ik} e_k \tag{11}$$

$$c_k = c_k + e_k \tag{12}$$

2.4. Extreme Learning Machine (ELM)

An ELM is a single-hidden layer feedforward neural network (SLFNN). The structure of an ELM is similar to that of a BPNN with a single hidden layer (Figure 4). Generally, we set the input matrix $\boldsymbol{X}$ and output matrix $\boldsymbol{Y}$ of the training set with Q samples as follows:

$$\boldsymbol{X} = \begin{bmatrix} x_{11} & x_{12} & \cdots & x_{1Q} \\ x_{21} & x_{22} & \cdots & x_{2Q} \\ \vdots & \vdots & & \vdots \\ x_{n1} & x_{n2} & \cdots & x_{nQ} \end{bmatrix}_{n\times Q} \quad \boldsymbol{Y} = \begin{bmatrix} y_{11} & y_{12} & \cdots & y_{1Q} \\ y_{21} & y_{22} & \cdots & y_{2Q} \\ \vdots & \vdots & & \vdots \\ y_{m1} & y_{m2} & \cdots & y_{mQ} \end{bmatrix}_{m\times Q} \tag{13}$$

According to the topological structure in Figure 4, the output $\boldsymbol{T}$ of the ELM network can be obtained as follows:

$$\boldsymbol{T} = [\boldsymbol{t}_1, \boldsymbol{t}_2, \cdots, \boldsymbol{t}_Q]_{m\times Q}, \boldsymbol{t}_j = \begin{bmatrix} t_{1j} \\ t_{2j} \\ \vdots \\ t_{mj} \end{bmatrix}_{m\times 1} = \begin{bmatrix} \sum\limits_{i=1}^{l} \beta_{i1} f(\boldsymbol{w}_i \boldsymbol{x}_j + b_i) \\ \sum\limits_{i=1}^{l} \beta_{i2} f(\boldsymbol{w}_i \boldsymbol{x}_j + b_i) \\ \vdots \\ \sum\limits_{i=1}^{l} \beta_{im} f(\boldsymbol{w}_i \boldsymbol{x}_j + b_i) \end{bmatrix} \tag{14}$$

where $j = 1, 2, \cdots, Q$, $\boldsymbol{w}_i = [w_{i1}, w_{i2}, \cdots, w_{in}]$, $x_j = \left[x_{1j}, x_{2j}, \cdots, x_{nj}\right]^T$, and $b = [b_1, b_2, \cdots, b_l]_{l\times 1}^T$.

Equation (14) is rewritten as follows:

$$\boldsymbol{H}\beta = \boldsymbol{T}' \tag{15}$$

where $\boldsymbol{H}$ is the output matrix of the hidden layer of the ELM neural network. The specific form is as follows:

$$\boldsymbol{H}(\boldsymbol{w}_1, \boldsymbol{w}_2, \cdots, \boldsymbol{w}_l, b_1, b_2, \cdots, b_l, \boldsymbol{x}_1, \boldsymbol{x}_2, \cdots, \boldsymbol{x}_Q) = \begin{bmatrix} f(\boldsymbol{w}_1 \cdot \boldsymbol{x}_1 + b_1) f(\boldsymbol{w}_2 \cdot \boldsymbol{x}_1 + b_2) f(\boldsymbol{w}_l \cdot \boldsymbol{x}_1 + b_l) \\ f(\boldsymbol{w}_1 \cdot \boldsymbol{x}_2 + b_1) f(\boldsymbol{w}_2 \cdot \boldsymbol{x}_2 + b_2) f(\boldsymbol{w}_l \cdot \boldsymbol{x}_2 + b_l) \\ \vdots \\ f(\boldsymbol{w}_1 \cdot \boldsymbol{x}_Q + b_1) f(\boldsymbol{w}_2 \cdot \boldsymbol{x}_Q + b_2) f(\boldsymbol{w}_l \cdot \boldsymbol{x}_Q + b_l) \end{bmatrix}_{Q\times l} \tag{16}$$

According to Theorem 1 proposed by Huang [39], if the number of neurons in the hidden layer is equal to the number of samples in the training set, the SLFNN can approach the training sample with zero error for any $\boldsymbol{w}$ and $\boldsymbol{b}$, as follows:

$$\sum_{j=1}^{Q} \left\| \boldsymbol{t}_j - \boldsymbol{y}_j \right\| = 0 \tag{17}$$

where $y_j = \left[y_{1j}, y_{2j}, \cdots, y_{mj}\right]^T (j = 1, 2, \cdots, Q)$.

In the case of a large number of samples (Q) in the training set, the number of neurons in hidden layer (K) is usually smaller than Q. It can be seen from the reference Theorem 2 [40] that the training error of SLFNN can be approximated to an arbitrary $\varepsilon > 0$, as follows:

$$\sum_{j=1}^{Q} \left\| \boldsymbol{t}_j - \boldsymbol{y}_j \right\| < \varepsilon \tag{18}$$

Therefore, when the activation function ($f(x)$) is infinitely differentiable, the parameters of SLFNN do not all need to be updated. $\boldsymbol{w}$ and $\boldsymbol{b}$ can be randomly selected before the training process and remain unchanged during the training process. $\boldsymbol{\beta}$ might be obtained by the least squares algorithm as follows:

$$\min_{\beta} \left\| \boldsymbol{H}\boldsymbol{\beta} - \boldsymbol{T}' \right\| \tag{19}$$

The solution of Equation (19) is as follows:

$$\hat{\boldsymbol{\beta}} = \boldsymbol{H}^{+}\boldsymbol{T}' \tag{20}$$

where $\boldsymbol{H}^{+}$ is the Moore–Penrose inverse of $\boldsymbol{H}$.

Therefore, the training process of ELM includes the following steps:

1. The number of neurons in the hidden layer is identified. $\boldsymbol{w}$ and $\boldsymbol{b}$ are randomly assigned.
2. An infinitely differentiable function is selected as the activation function of the hidden layer neurons, and then the output matrix ($\boldsymbol{H}$) of the hidden layer is obtained.
3. The weight matrix ($\hat{\boldsymbol{\beta}}$) of the output layer is determined.

2.5. Multiple Linear Regression (MLR)

MLR is a straightforward statistical method that allows for establishing the linear relationship that occurs between one dependent, response variable (the flow regime index of each studied SWRLC emitter in this work) and a number of independent, explanatory variables (data of key structural parameters of the SWRLC emitter flow channel here) through a set of coefficients β. In other words, the MLR model is used to find a higher-dimensional plane that best represents the dataset. MLR with n explanatory variables can be expressed as follows:

$$y = \beta_0 + \beta_1 x_1 + \beta_2 x_2 + \cdots + \beta_n x_n \tag{21}$$

where y is the response variable, $x_1, x_2, \cdots, x_n$ are explanatory variables, and the regression coefficients β_i reflect the amount of change in y caused by a change in unit x when other variables are constant. Since both the response and explanatory variables are known, these coefficients can be adjusted by minimizing the residual sum of squares as follows:

$$\sum_i \left[y_i - (\beta_0 + \beta_1 x_{1,i} + \beta_2 x_{2,i} + \cdots + \beta_n x_{n,i})\right]^2 \tag{22}$$

The standard error (SE), t statistic (t-stat), and probability (p-value) of explanatory variables are evaluated, as it is important to estimate these regression coefficients. The performance of the MLR model is examined by two key indicators (r^2_{MLR} and p-value). r^2_{MLR} represents what percentage of variation in response variable can be explained by the MLR model. Significance level (p-value) quantifies the probability that the difference between sample and hypothetical population is caused by chance. The p-value was 0.05 in this study.

2.6. Assessment Indices

It is obvious that prediction itself has uncertainties connected with data acquisition and processing and model precision. The difference between the observed and estimated data is called model error. In this study, root mean square error (RMSE), mean absolute error (MAE), mean bias error (MBE), coefficient of determination (R^2), and the comprehensive indicator (CI) were introduced to evaluate the performance of the abovementioned models. The five indicators are described below.

2.6.1. Root Mean Square Error (RMSE)

The RMSE, also known as the standard error, is the square root of the ratio of the square of the deviation between predicted and observed values to the number of samples [41]. The RMSE is sensitive to very small or large errors in a set of data, so it can reflect the forecasting accuracy of model. The smaller the value of the RMSE, the better the performance of the model. It can be expressed as follows:

$$\mathrm{RMSE} = \sqrt{\frac{\sum_{i=1}^{n} (O_i - P_i)^2}{n}} \tag{23}$$

where O_i and P_i are the values of observed and predicted data, respectively. n is the total number of observed flow regime indices.

2.6.2. Mean Absolute Error (MAE)

The mean absolute error (MAE) is the average of the absolute value of the deviation from the arithmetic mean of all individual predicted values [42]. More significantly, the MAE is less affected by outliers. Therefore, it can better reflect the actual situation of the predicted value error. The MAE might be obtained as follows:

$$\mathrm{MAE} = \frac{\sum_{i=1}^{n} |O_i - P_i|}{n} \tag{24}$$

2.6.3. Mean Bias Error (MBE)

Mean bias error (MBE) is applied when evaluating the overestimation (positive value) and underestimation (negative value) of a model [43]. In this study, a positive value means that the model overestimates the flow regime index, while a negative value means that it underestimates it. The more accurate the model, the closer the MBE is to zero. The defect of MBE is that it cannot reflect the correct performance when the model presents overestimated and underestimated values at the same time. The MBE can be expressed as follows:

$$\mathrm{MBE} = \frac{\sum_{i=1}^{n} (P_i - O_i)}{n} \tag{25}$$

2.6.4. Coefficient of Determination (R^2)

The coefficient of determination (R^2), also known as goodness of fit, reflects the proportion of variation in dependent variable that can be explained by the model [43]. The R^2 determines the degree of correlation, and it ranges from zero to one. The larger the value of R^2, the denser the predicted points near the regression line. This index examines the linearity, and it is extremely helpful for improving the performance of the model. The R^2 can be obtained as follows:

$$R^2 = \left[\frac{\sum_{i=1}^{n} (O_i - \overline{O})(P_i - \overline{P})}{\sqrt{\sum_{i=1}^{n} (O_i - \overline{O})^2 \sum_{i=1}^{n} (P_i - \overline{P})^2}} \right]^2 \quad (26)$$

where $\overline{O}$ and $\overline{P}$ are the mean values of observed and predicted flow regime indices.

2.6.5. Comprehensive Indicator (CI)

Over the past decades, many researchers have investigated the prediction of hydraulic performance of drip irrigation emitters. Most of the scholars have chosen RMSE and MBE to test the accuracy of the models. Each indicator has its own advantages and disadvantages. Therefore, one or two indicators cannot be used to determine whether a model is good or bad. Inspired by Behar [43], a new evaluation index, called the comprehensive indicator (CI), was introduced, as illustrated in Equation (27). The CI is a multiplication of four statistical indices. CI comprehensively considers the advantages of the four indicators mentioned above. The greatest advantage of CI is that evaluating the performance of models become more comprehensive and realistic. The higher the model precision, the closer the CI value is to 0.

$$\mathrm{CI} = \mathrm{RMSE} \times \mathrm{MAE} \times \mathrm{MBE} \times \left(1 - R^2\right) \quad (27)$$

2.7. Experimental Procedure

The SWRLC emitter products were manufactured by electrical discharge machining (EDM) and injection molding. The manufacturing processes are shown in Figure 5. The molds of the SWRLC emitter were manufactured by EDM, and its products were realized using injection molding.

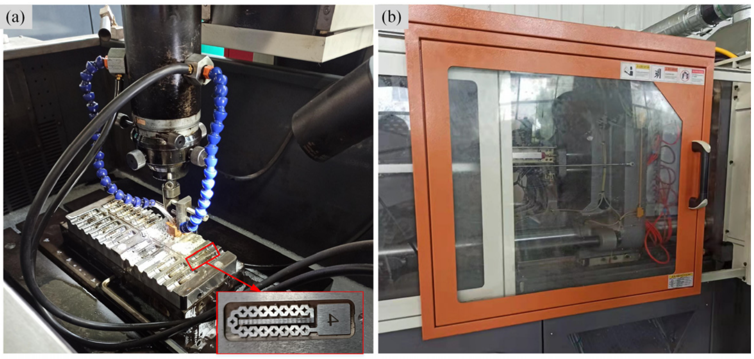

Figure 5. The manufacturing processes of the SWRLC emitter: (**a**) mold manufacturing by EDM; (**b**) injection molding production.

For conducting the experiments, the hydraulic performance test bench was built at the Advanced Manufacturing Laboratory at Shandong University [35,37], as shown in Figure 6. This test bench consists of a pressure gauge (the precision is at the 0.4 level and the measuring range is 0~0.6 MPa; Xiyi Group Co., Ltd., Xi'an, China), a test area for irrigation emitters, several measuring cups (the volume is 2000 mL), an electronic weighing scale (the precision is 0.1 g and the measuring range is 0~10 kg; Shenzhen Qianxue Electronics Co., Ltd., Shenzhen, China), as well as a data acquisition unit and a pressure regulating valve. A total of 25 emitters were randomly selected to be connected to the testing region of the emitters. In the test, tap water was selected as the test water, and its temperature was about 18 °C. During the experiment, the outlet flow of the emitters was measured every three minutes under different pressures (20–180 kPa, at intervals of 40 kPa). The experimental results take the average of the two measured flow results as the final value.

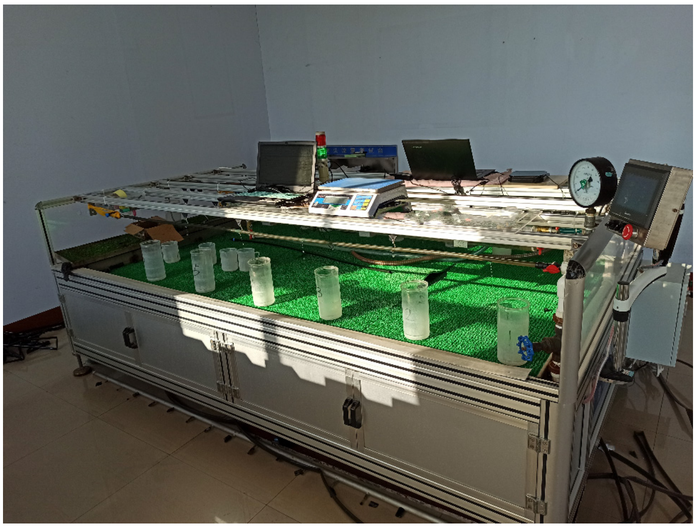

Figure 6. Laboratory experimental platform for measured emitter discharge.

3. Results

3.1. CFD Simulated Data Verification

To examine the reliability of CFD simulated data, a set of key parameter combinations of the SWRLC emitter was randomly selected and manufactured by EDM technology and the IM method. SWRLC emitters selected the drip belts with a 16 mm inner diameter and 0.3 mm wall thickness. The distance between SWRLC emitters on drip belts was 40 cm. The physical models of the SWRLC emitter and drip belts are shown in Figure 7.

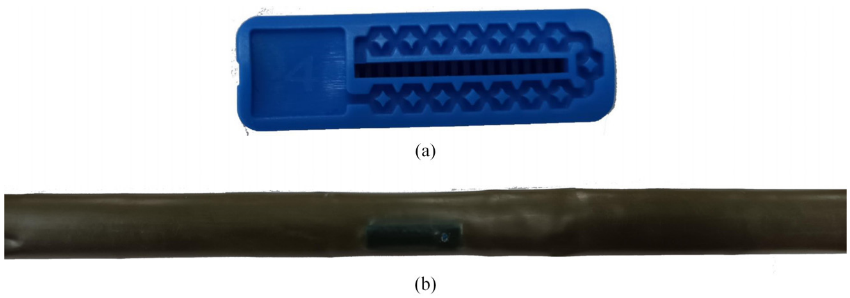

Figure 7. (**a**) SWRLC emitter; (**b**) drip irrigation belts.

The simulated and test results of the SWRLC emitter are listed in Table 2, from which it can be seen that the discharge of the SWRLC emitter rose with the increase in working pressure. The error between simulated discharge and measured discharge of the SWRLC emitter was about 0.2 L/h. The simulated and measured flow regime indices were 0.477 and 0.472, respectively. The errors between the simulated data and measured data were very small based on the above analysis. Therefore, in order to shorten the development time and save economic costs, the CFD simulated data, named as observed data, was used for the establishment of the dataset in this study.

Table 2. Hydraulic performance statistics of SWRLC emitter.

Items	Flow Rate (L/h)					x
	20 kPa	60 kPa	100 kPa	140 kPa	180 kPa	
Simulations	3.257	5.521	7.044	8.276	9.348	0.477
Measurements	3.449	5.651	7.237	8.499	9.626	0.472

3.2. Analysis and Division Data

Many studies have shown that the geometrical parameters of a flow channel play an important role in the values and changes in the flow regime index of an emitter [44]. Therefore, the length of the trapezoid baseline, angle between the hypotenuses of adjacent trapezoids, trapezoid height, radius of stellate water-retaining structure, spacing of two symmetric trapezoids, path depth, and SWRLC unit number were used as input parameters. The flow regime index x was the model's output. A total of 135 samples were collected, and the numerical characteristics of the dataset are presented in Table 3.

Table 3. Numerical characteristics of the dataset.

Parameter	Minimum	Maximum	Median	Mean	SD	CV	Skewness	Kurtosis
s (mm)	2.10	2.50	2.30	2.2822	0.1481	6.49	0.1417	−1.3886
θ (°)	20	60	40	39.7778	14.0078	35.22	0.0069	−1.2690
h (mm)	0.60	1.00	0.80	0.7948	0.1411	17.75	0.0440	−1.2870
r (mm)	0.60	1.00	0.80	0.7956	0.1392	17.50	0.0295	−1.2574
a (mm)	0.45	0.65	0.55	0.5481	0.0706	12.87	0.0177	−1.2899
d (mm)	0.90	1.30	1.10	1.0933	0.1399	12.80	0.0534	−1.2644
n	10	19	15	14.6889	2.8741	19.57	0.1114	−1.2425
x	0.4779	0.5023	0.4905	0.4907	0.0049	1.010	−0.0202	−0.3256

Among all of the parameters, the θ and a showed the maximum and minimum mean values of 39.7778 and 0.5481, respectively. θ and x showed the maximum and minimum standard deviation (SD) values of 14.0078 and 0.0049, respectively. Since the units and mean values of all of the parameters were different, coefficient of variation (CV) was used instead of standard deviation to measure the degree of variation. It can be seen from Table 2 that θ had highest data deviation (35.22) from the mean values, followed by n (19.57). Since the mean values and CV values of some parameters were very different, the dataset was normalized before model training so that its characteristics were all of the same order of magnitude. This was beneficial to improve the predictive accuracy of the model and shorten the training time. Nonetheless, the severely skewed data distribution indicates that the data is abnormal and may affect the predictive performance of the machine learning model. Skewness is a numerical characteristic of the asymmetrical degree of the data distribution. Generally, the skewness is between −0.5 and 0.5, indicating that the data is approximating symmetry. Table 3 showed that all the input parameters had a positively skewed distribution, and the output parameter (the flow regime index) had a negatively skewed distribution. The s and a showed the maximum and minimum skewness values of 0.1417 and −0.0202, respectively. The skewness values of all parameters were in the range of −0.5 to 0.5, which indicated that the data distribution was approximating symmetry. In order to intuitively check the data distribution of each parameter, the quantile–quantile plots of seven input variables and an output variable are shown in Figure 8. It is obvious that the dataset had a normal distribution based on the results of the quantile–quantile plots. In addition, the values of the skewness and kurtosis for each parameter were small.

A vast amount of data is required to acquire a high-precision machine learning model. It is also crucial to input typical data so that the model learns and obtains more available information. The data of seven variables were randomized and divided into training and testing subsets. In this study, the original dataset was divided into training and testing dataset in a ratio of 7:3 [45]. Then, the model was trained by the training dataset (95 samples), and its accuracy was evaluated by the testing dataset (40 samples).

3.3. Performance of BPNN Model

In this study, the influences of different transfer functions and the number of hidden layer neurons on the BPNN model performance were studied. The RMSE, MAE, MBE, and R^2 values were verified as the number of hidden layer neurons in the BPNN model increased, as shown in Figure 9. The performance of the BPNN model prominently improved with the increase in the number of neurons in the hidden layer, as reflected in the values of the four evaluation indices for three activation functions. The low values of RMSE and MAE, the high values of R^2, and the values of MBE close to zero, manifesting good performance, were achieved by increasing the hidden neurons to more than eight. It can be seen from Figure 9 that the performance of the Tansig function was better than that of the Logsig and Hardlim functions for flow regime index x. When Tansig function was used and the number of hidden layer neurons was 10, there was an obvious improvement in the BPNN model for flow regime index x. The RMSE and MAE were 0.00188 and 0.00148, respectively. The MBE and R^2 were 1.0342×10^{-4} and 88.50%, respectively. The CI was 3.32×10^{-11} at this point which was closest to zero. The optimal BPNN architecture was 7–10–1 (input neurons, hidden neurons, and output neuron, respectively) with the Tansig function, as the best x prediction was achieved. The developed BPNN architecture is shown in Figure 10.

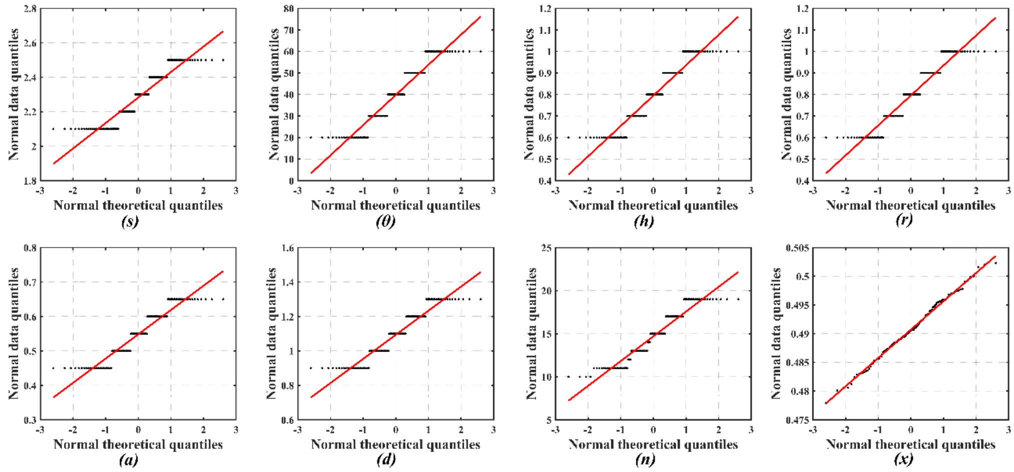

Figure 8. Quantile–quantile plot of the dataset.

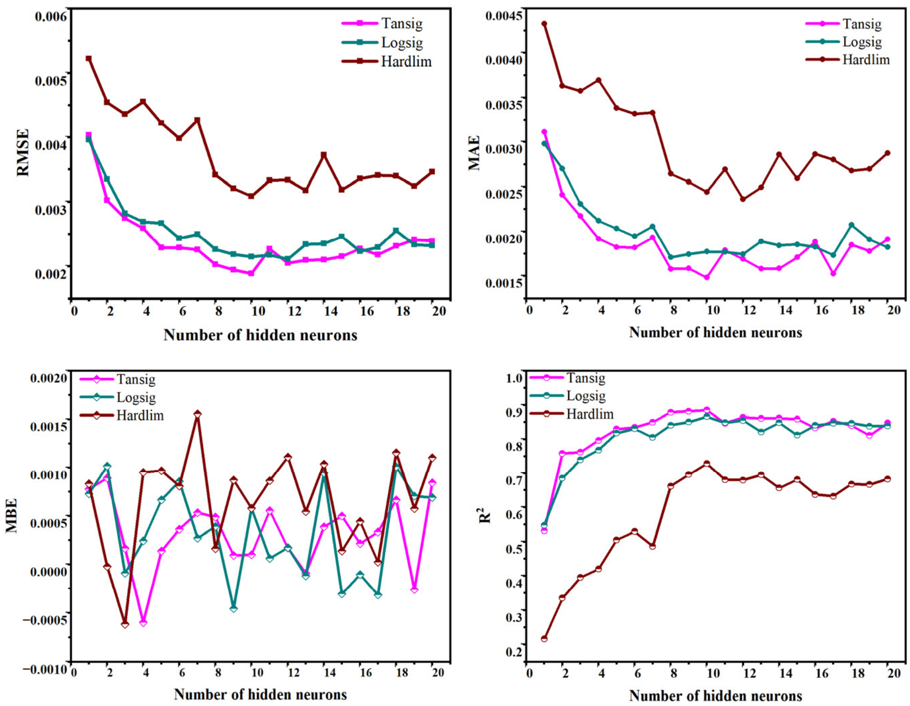

Figure 9. Statistical performance of the BPNN model with different transfer functions and hidden neurons in the testing stage.

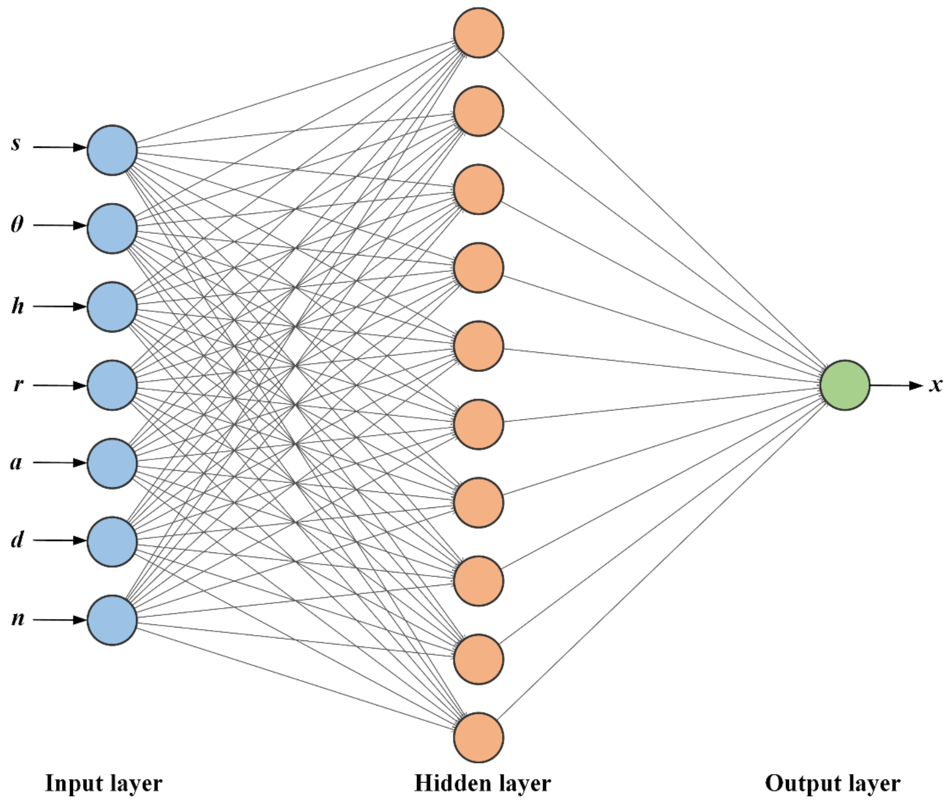

Figure 10. Optimal architecture of the developed BPNN model.

3.4. Performance of ELM Model

The influences of different transfer functions and the number of neurons in hidden layer on ELM model were also studied in order to determine the optimal model structure. In the training process, when the number of neurons in the hidden layer ranges from 1 to 10, the model gave a poor x prediction (the values of RMSE and MAE were too large, the value of MBE was too far from 0, and the value of R^2 was too small). Figure 11 demonstrated that increasing the number of hidden layer neurons from 10 to 40 generated a conspicuous improvement in ELM model performance using 3 functions for x. The Tansig function performed best among the three activation functions. The values of RMSE and MAE were firstly decreased and then increased with the rise in the number of hidden layer neurons. The value of RBE oscillated around zero and the value of R^2 firstly increased and then decreased as the number of hidden neurons increased. In particular, the value of CI was 1.96×10^{-11} (the lowest) when the number of neurons in the hidden layer was 37 and the Tansig function was used. The RMSE and MAE at this point were 0.00163 and 0.00126, respectively. The MBE and R^2 were 1.128×10^{-4} and 91.49%, respectively. Therefore, the most appropriate ELM model structure was 7–37–1 (input neurons, hidden neurons, and output neuron, respectively), which gave the best performance for predicting flow regime index x. The proposed ELM model structure is shown in Figure 12.

3.5. Performance of MLR Model

The MLR model had been used by some scholars to study the prediction of drip irrigation emitter discharge. The MLR model was established to confirm the predicted ability of the proposed BPNN and ELM model. The MLR model for flow regime index x was developed by employing the training dataset (95 samples). The best fitting formula of the MLR model as follows:

$$x = 0.46444 + 0.00969s + 0.000134\theta + 0.01494h - 0.01317r + 0.02174a - 0.00291d - 0.000754n \quad (28)$$

The SE, *t*-stat, *p*-value, F and VIF of input parameters, and r^2_{MLR} of the MLR model are presented in Table 4. The *t*-stat absolute values of all independent variables were greater than 2 except d (−1.885), indicating that these parameters had a large contribution to the MLR model for x. The *p*-value also illustrated this phenomenon. The *p*-value of d was 6.84×10^{-2} ($p > 0.05$), manifesting that it was not significantly affected. The n was the most significant independent variable, followed by h. The VIF values of all independent variables were less than 5 due to the weak linear relationship between them. In addition, Table 4 indicated that the r^2_{MLR} of the MLR model was 85.76%, confirming the goodness of fit. The fitted MLR model was employed for prediction using the testing dataset (40 samples). The indicators RMSE, MAE, MBE, and R^2, reflecting the predicted performance of the MLR model, are presented in Table 5.

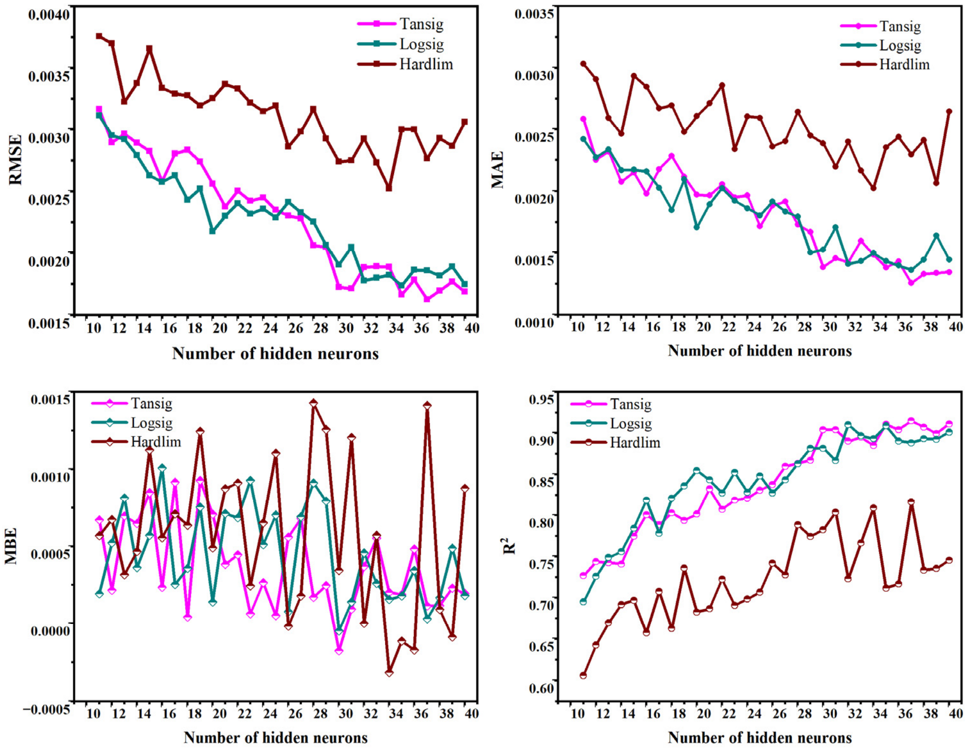

Figure 11. Statistical performance of the ELM model with different transfer functions and hidden neurons in the testing stage.

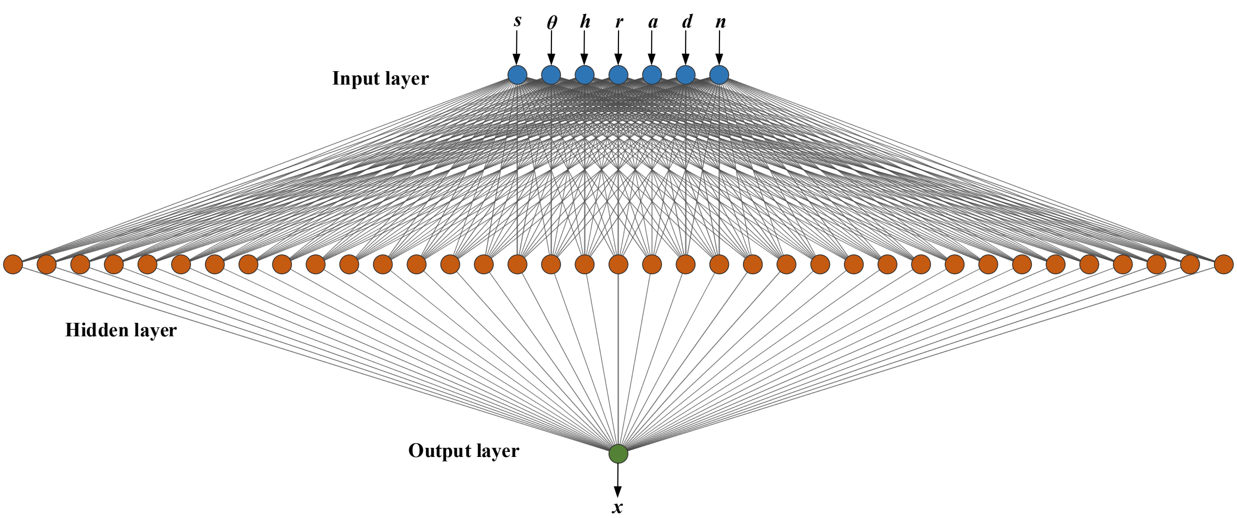

Figure 12. Most appropriate structure of the proposed ELM model.

Table 4. Regression analysis of independent variables for the MLR model.

Items	SE	*t*-Stat	*p*-Value	F	VIF	r^2_{MLR}
Intercept	0.004694	98.95	0	-	-	-
s	0.001593	6.086	8.38×10^{-8}	37.04	1.16	-
θ	0.000016	8.391	9.39×10^{-12}	70.40	1.11	-
h	0.001672	8.938	1.09×10^{-12}	79.88	1.14	-
r	0.001539	−8.559	4.83×10^{-12}	73.26	1.05	-
a	0.003274	6.642	9.52×10^{-9}	44.12	1.11	-
d	0.001571	−1.855	6.84×10^{-2}	3.441	1.11	-
n	0.000073	−10.380	4.20×10^{-15}	107.7	1.08	-
MLR	-	-	-	-	-	85.76%

Table 5. Statistical prediction performance of the MLR model.

Model	RMSE	MAE	MBE	R^2
MLR	0.00404	0.00287	0.00081	51.08%

3.6. Comparison of Developed Models

Figure 13 indicated that ELM model with the lowest RMSE and MAE values (0.00163 and 0.00126, respectively) and highest R^2 value (91.49%) performed better than the others. The MBE value ranked the BPNN model performance (1.03×10^{-4}) as excellent followed by ELM model. It is testified that different assessment indices may bring about a different evaluation result of model performance since each assessment indicator had a specific evaluation level. The choice of model with best performance based on the different assessment indicator was not a responsible method.

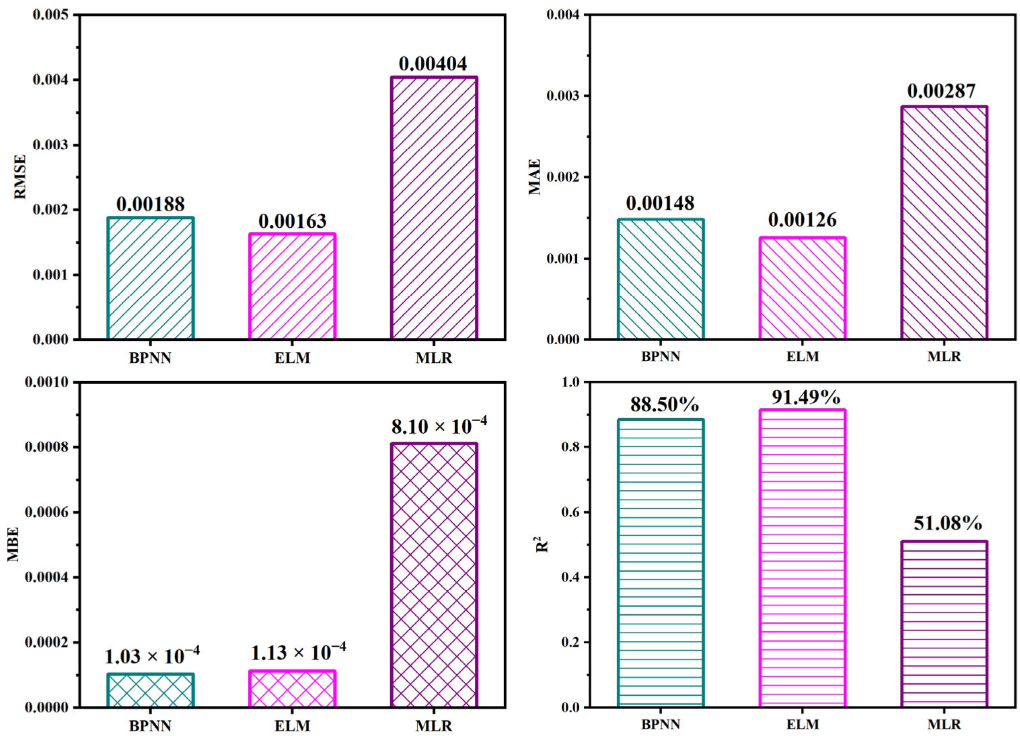

Figure 13. The test phase performance indicators of three best developed models.

Therefore, the CI index was introduced and used in this study to overcome this problem. The model with minimum CI value (near zero) was superior in performance than others. The MLR model had worst performance in predicting the parameter of flow regime index x with CI = 4.84×10^{-9}. The MLR model was not evaluated by CI index shown in Figure 14 on account of presenting CI > 10^{-10}. The CI values of developed BPNN and ELM models were shown in Figure 14. The ELM model performed best performance with CI = 1.96×10^{-11} followed by the BPNN model. The introduced CI index eliminated any doubts about the selection of high performance and quality model.

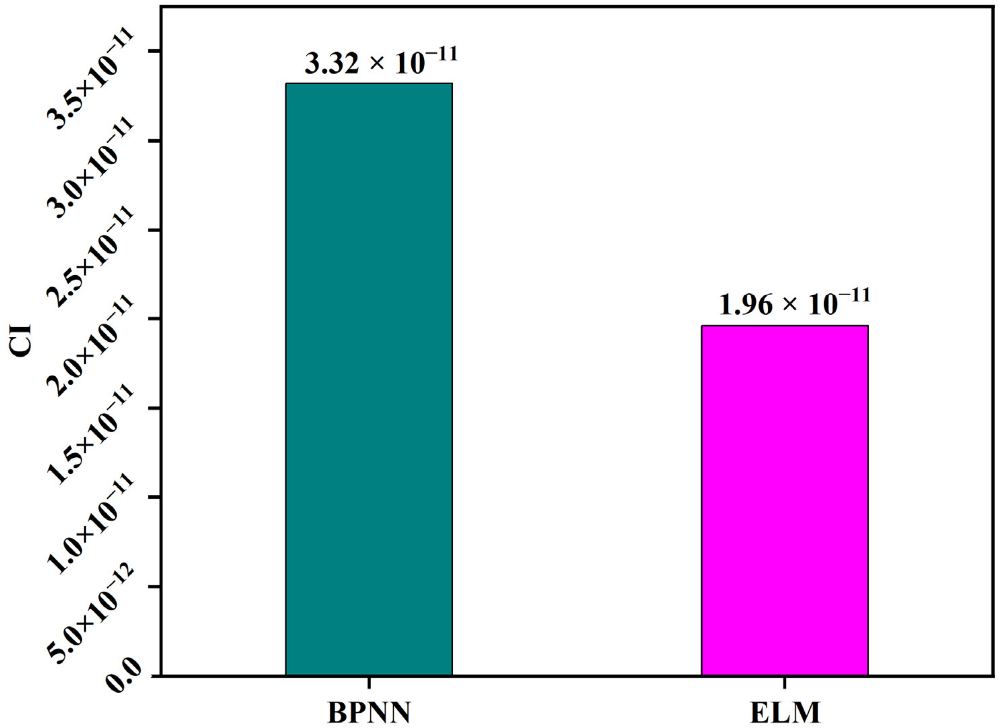

Figure 14. The CI values of the developed BPNN and ELM models.

Next, the errors that equaled differences between the predicted and observed values were compared, as shown in Figure 15. The distribution in Figure 15 showed that the errors of the three models were concentrated around zero. The median value of the ELM model was 0.00008, which was lower than the BPNN (Q2 = 0.00028) and MLR (Q2 = 0.00028). This indicated that the average level of ELM error was closer to 0. In other words, the predicted values of the ELM were closer to the observed values. The interquartile range (IQR) for ELM, BPNN, and MLR were 0.00196, 0.00248, and 0.00412, respectively. In the lower quartile, the ELM with Q1 = −0.00058 performed better than BPNN (Q1 = −0.00116) and MLR (Q1 = −0.00177). Additionally, the upper quartile in BPNN (Q3 = 0.00132) was lowest, followed by ELM with a slight difference (△Q3 = 0.00006). Figure 14 showed that the lower and upper edge values in the ELM model (−0.00298 and 0.00302, respectively) were lower than in the BPNN model (−0.0047 and 0.00361, respectively) and the MLR model (−0.00478 and 0.00754, respectively), confirming the ability of the ELM model to predict flow regime index x.

Finally, the Taylor diagram was employed to intuitively compare the performance of the three developed models. Due to the smaller standard deviation (SD) and RMSE values, the values expand by a factor of 1000 in Figure 16. The ELM model had the smallest difference with the standard deviation of observed flow regime index x values. In the RMSE index, the ELM and BPNN models were in the first radius relative to the observed point, while the MLR model was not, and the ELM model had the smallest distances. In addition, the correlation coefficient of the ELM model was greater than 0.95, and the others were less than 0.95. Therefore, the ELM model had excellent ability to build relationship between key parameters of the labyrinth channel and flow regime index by the above analyses.

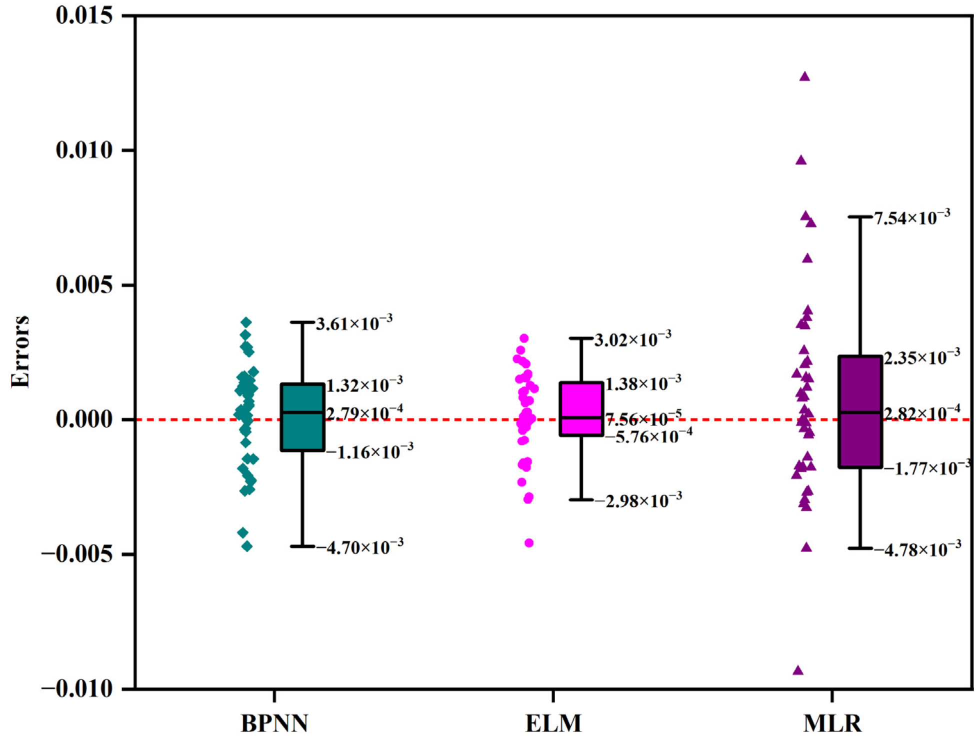

Figure 15. The boxplot of errors distribution of the three developed models in the test stage.

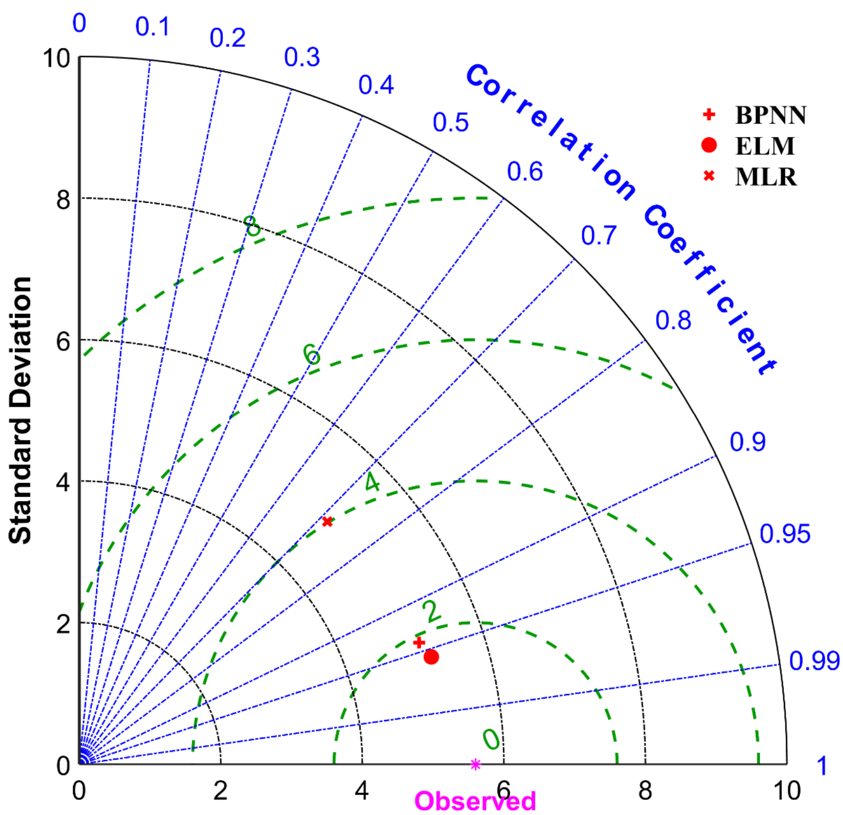

Figure 16. The Taylor diagram showing a comparison of the three developed models.

4. Discussion

The flow regime index is an important indicator to measure irrigation uniformity of a drip irrigation emitter, and it is mainly determined by the structural parameters of the emitter. Generally, the flow regime index of the emitter is obtained in two steps: the first is to measure the flow under different working pressures; the second is to obtain the flow regime index by fitting the flow and pressure with the empirical formula. If CFD simulation is carried out, grid division and simulation calculation are required. Using a high-performance computer (Intel(R)Core(TM) i9-10900K CPU @3.70GHz), it takes about 6 h to obtain the flow regime index of a set of structural size SWRLC emitters. If the processing test, the emitter processing cost, the drip irrigation tape cost, the test bench cost, the processing cycle time, and the test time are to be considered, this process requires a lot of time and money. The ELM model established in this study based on machine learning technology can directly describes the relationship between a SWRLC's structural parameters and its flow mode index. This can greatly save time and economic costs in the design phase of a SWRLC emitter, which is conducive to rapid development. This is also beneficial for water-saving irrigation.

In this paper, the models were built based on all structural parameters as the inputs, so the seven input variables are not compared. It is not necessarily true that the more input variables, the better the effect of the model. In the future, different combinations of inputs variables can be considered to further expand the data set, and the predictive performance of other machine learning models can also be explored.

5. Conclusions

The main purpose of this study is to establish the relationship between the flow channel structure parameters and its flow regime index based on machine learning technologies, the CFD method, and experimental study for rapid, efficient, and low-cost design and development of novel types of emitters. In this study, the ELM, BPNN, and MLR models were developed to predict flow regime index x of the novel SWRLC emitter. The hydraulic performance test results showed that the CFD simulation had high reliability. In order to address the problem of different evaluation results of existing assessment indices, the CI index was introduced. Based on the obtained results, the architectures of best performance of ELM and BPNN models were 7–37–1 and 7–10–1, respectively. The results showed that the performance of the ELM model with a minimum CI value (1.96×10^{-11}) was superior to the other models. In the design and development stage of the emitters, the flow regime index can be obtained by directly inputting the structural parameters of the emitters into the trained ELM model. The findings of this study showed that the ELM model can be a good substitute for laboratory and field measurements to obtain the flow regime index x of a SWRLC emitter in the design and development stage, saving both time and money and increasing efficiency.

Author Contributions: Conceptualization, Y.L. and X.F.; methodology, Y.L., X.H. and Y.S.; software, Y.L.; validation, Y.L. and X.H.; formal analysis, Y.L. and X.F.; investigation, Y.L., X.H. and Y.S.; resources, X.F.; data curation, Y.L. and X.H.; writing—original draft preparation, Y.L.; writing—review and editing, Y.L., X.F. and H.L.; visualization, Y.L.; supervision, X.F. and H.L.; project administration, X.F. and H.L.; funding acquisition, X.F. All authors have read and agreed to the published version of the manuscript.

Funding: This research was funded by [Key Research and Development Plan of Shandong Province] grant number [2020CXGC010807] and the APC was funded by [Key Research and Development Plan of Shandong Province (2020CXGC010807)].

Data Availability Statement: The study did not report any data.

Acknowledgments: We are grateful for the financial support from the Key Research and Development Plan of Shandong Province (grant number 2020CXGC010807).

Conflicts of Interest: The authors declare that they have no known competing financial interests or personal relationships that could have appeared to influence the work reported in this paper.

References

1. Lamm, F.R.; Colaizzi, P.D.; Sorensen, R.B.; Bordovsky, J.P.; Dougherty, M.; Balkcom, K.; Zaccaria, D.; Bali, K.M.; Rudnick, D.R.; Peters, R.T. A 2020 Vision of Subsurface Drip Irrigation in the U.S. *Trans. ASABE* **2021**, *64*, 1319–1343. [CrossRef]
2. Nogueira, V.H.B.; Diotto, A.V.; Thebaldi, M.S.; Colombo, A.; Silva, Y.F.; Lima, E.M.D.C.; Resende, G.F.L. Variation in the Flow Rate of Drip Emitters in a Subsurface Irrigation System for Different Soil Types. *Agric. Water Manag.* **2021**, *243*, 106485. [CrossRef]
3. Ait-Mouheb, N.; Schillings, J.; Al-Muhammad, J.; Bendoula, R.; Tomas, S.; Amielh, M.; Anselmet, F. Impact of Hydrodynamics On Clay Particle Deposition and Biofilm Development in a Labyrinth-Channel Dripper. *Irrig. Sci.* **2019**, *37*, 1–10. [CrossRef]
4. Li, Y.; Feng, J.; Xue, S.; Muhammad, T.; Chen, X.; Wu, N.; Li, W.; Zhou, B. Formation Mechanism for Emitter Composite-Clogging in Drip Irrigation System. *Irrig. Sci.* **2019**, *37*, 169–181. [CrossRef]
5. Peng, H.; Shuqin, L.; Zeyuan, L.; Hongxu, Z.; Muhammd, T.; Ruonan, W.; Wenchao, L.; Yunkai, L. Water Temperature Effects On Hydraulic Performance of Pressure-Compensating Emitter in a Drip Irrigation System. *Irrig. Drain.* **2021**, *70*, 332–341. [CrossRef]
6. Yang, B.; Wang, J.; Zhang, Y.; Wang, H.; Ma, X.; Mo, Y. Anti-Clogging Performance Optimization for Dentiform Labyrinth Emitters. *Irrig. Sci.* **2020**, *38*, 275–285. [CrossRef]
7. Yu, L.; Li, N.; Long, J.; Liu, X.; Yang, Q. The Mechanism of Emitter Clogging Analyzed by CFD-DEM Simulation and PTV Experiment. *Adv. Mech. Eng.* **2018**, *10*, 1687814017743025. [CrossRef]
8. Feng, J.; Li, Y.; Wang, W.; Xue, S. Effect of Optimization Forms of Flow Path On Emitter Hydraulic and Anti-Clogging Performance in Drip Irrigation System. *Irrig. Sci.* **2018**, *36*, 37–47. [CrossRef]
9. Xu, T.; Zhang, L. Influence and Analysis of Structure Design and Optimization On the Performance of a Pit Drip Irrigation Emitter. *Irrig. Drain.* **2020**, *69*, 633–645. [CrossRef]
10. Guo, L.; Bai, D.; Zhou, W.; Wang, X. Evaluation of Numerical Simulation Accuracy for Two-Ways Mixed Flow Drip Irrigation Emitter Based On CFD. *Int. J. Heat Technol.* **2017**, *35*, 384–392. [CrossRef]
11. Xing, S.; Wang, Z.; Zhang, J.; Liu, N.; Zhou, B. Simulation and Verification of Hydraulic Performance and Energy Dissipation Mechanism of Perforated Drip Irrigation Emitters. *Water* **2021**, *13*, 171. [CrossRef]
12. Al-Amoud, A.I.; Mattar, M.A.; Ateia, M.I. Impact of Water Temperature and Structural Parameters On the Hydraulic Labyrinth-Channel Emitter Performance. *Span. J. Agric. Res.* **2014**, *12*, 580–593. [CrossRef]
13. Yu, L.; Li, N.; Liu, X.; Yang, Q.; Li, Z.; Long, J. Influence of Dentation Angle of Labyrinth Channel of Drip Emitters on Hydraulic and Anti-Clogging Performance. *Irrig. Drain.* **2019**, *68*, 256–267. [CrossRef]
14. Zhangzhong, L.; Yang, P.; Li, Y.; Ren, S. Effects of Flow Path Geometrical Parameters On Flow Characteristics and Hydraulic Performance of Drip Irrigation Emitters. *Irrig. Drain.* **2016**, *65*, 426–438. [CrossRef]
15. Zhang, J.; Zhao, W.; Lu, B. Rapid Prediction of Hydraulic Performance for Emitters with Labyrinth Channels. *J. Irrig. Drain. Eng.* **2013**, *139*, 414–418. [CrossRef]
16. Yang, C.; Gabbouj, M.; Jia, M.; Li, Z. Hierarchical Symbol Transition Entropy: A Novel Feature Extractor for Machinery Health Monitoring. *IEEE Trans. Ind. Inform.* **2022**, *18*, 6131–6141. [CrossRef]
17. Wang, L.; Guo, Y.; Fan, M.; Li, X. Wind Speed Prediction Using Measurements From Neighboring Locations and Combining the Extreme Learning Machine and the AdaBoost Algorithm. *Energy Rep.* **2022**, *8*, 1508–1518. [CrossRef]
18. Chatterjee, S.; Thakur, R.S.; Yadav, R.N.; Gupta, L. Sparsity-Based Modified Wavelet De-Noising Autoencoder for ECG Signals. *Signal Process.* **2022**, *198*, 108605. [CrossRef]
19. Razmi, M.; Saneie, M.; Basirat, S. Estimating Discharge Coefficient of Side Weirs in Trapezoidal and Rectangular Flumes Using Outlier Robust Extreme Learning Machine. *Appl. Water Sci.* **2022**, *12*, 176. [CrossRef]
20. Sadgrove, E.J.; Falzon, G.; Miron, D.; Lamb, D.W. The Segmented Colour Feature Extreme Learning Machine: Applications in Agricultural Robotics. *Agronomy* **2021**, *11*, 2290. [CrossRef]
21. Aqel, D.; Al-Zubi, S.; Mughaid, A.; Jararweh, Y. Extreme Learning Machine for Plant Diseases Classification: A Sustainable Approach for Smart Agriculture. *Clust. Comput.* **2022**, *25*, 2007–2020. [CrossRef]
22. Li, Y.; Feng, X.; Liu, Y.; Han, X. Apple Quality Identification and Classification by Image Processing Based On Convolutional Neural Networks. *Sci. Rep.* **2021**, *11*, 16618. [CrossRef] [PubMed]
23. Gao, F.; Fang, W.; Sun, X.; Wu, Z.; Zhao, G.; Li, G.; Li, R.; Fu, L.; Zhang, Q. A Novel Apple Fruit Detection and Counting Methodology Based On Deep Learning and Trunk Tracking in Modern Orchard. *Comput. Electron. Agric.* **2022**, *197*, 107000. [CrossRef]
24. Nguyen, T.T.; Ngo, H.H.; Guo, W.; Chang, S.W.; Nguyen, D.D.; Nguyen, C.T.; Zhang, J.; Liang, S.; Bui, X.T.; Hoang, N.B. A Low-Cost Approach for Soil Moisture Prediction Using Multi-Sensor Data and Machine Learning Algorithm. *Sci. Total Environ.* **2022**, *833*, 155066. [CrossRef]
25. Adongo, T.A.; Abagale, F.K.; Agyare, W.A. Modelling and Forecasting Reservoir Sedimentation of Irrigation Dams in the Guinea Savannah Ecological Zone of Ghana. *Water Pract. Technol.* **2021**, *16*, 1355–1369. [CrossRef]
26. Wan, X.; Li, B.; Chen, D.; Long, X.; Deng, Y.; Wu, H.; Hu, J. Irrigation Decision Model for Tomato Seedlings Based On Optimal Photosynthetic Rate. *Int. J. Agric. Biol. Eng.* **2021**, *14*, 115–122. [CrossRef]
27. Trejo-Alonso, J.; Fuentes, C.; Chávez, C.; Quevedo, A.; Gutierrez-Lopez, A.; González-Correa, B. Saturated Hydraulic Conductivity Estimation Using Artificial Neural Networks. *Water* **2021**, *13*, 705. [CrossRef]
28. Kumar, N.; Adeloye, A.J.; Shankar, V.; Rustum, R. Neural Computing Modelling of the Crop Water Stress Index. *Agric. Water Manag.* **2020**, *239*, 106259. [CrossRef]

29. Wang, Y.; Liu, L.; Guo, P.; Zhang, C.; Zhang, F.; Guo, S. An Inexact Irrigation Water Allocation Optimization Model Under Future Climate Change. *Stoch. Environ. Res. Risk Assess.* **2019**, *33*, 271–285. [CrossRef]
30. Mattar, M.A.; Alamoud, A.I. Artificial Neural Networks for Estimating the Hydraulic Performance of Labyrinth-Channel Emitters. *Comput. Electron. Agric.* **2015**, *114*, 189–201. [CrossRef]
31. Lavanholi, R.; de Camargo, A.P.; Avila Bombardelli, W.W.; Frizzone, J.A.; Ait-Mouheb, N.; da Silva, E.A.; de Oliveira, F.C. Prediction of Pressure-Discharge Curves of Trapezoidal Labyrinth Channels from Nonlinear Regression and Artificial Neural Networks. *J. Irrig. Drain. Eng.* **2020**, *146*, 04020018. [CrossRef]
32. Mattar, M.A.; Alamoud, A.I. Gene Expression Programming Approach for Modeling the Hydraulic Performance of Labyrinth-Channel Emitters. *Comput. Electron. Agric.* **2017**, *142*, 450–460. [CrossRef]
33. Seyedzadeh, A.; Maroufpoor, S.; Maroufpoor, E.; Shiri, J.; Bozorg-Haddad, O.; Gavazi, F. Artificial Intelligence Approach to Estimate Discharge of Drip Tape Irrigation Based On Temperature and Pressure. *Agric. Water Manag.* **2020**, *228*, 105905. [CrossRef]
34. Mattar, M.A.; Alamoud, A.I.; Al-Othman, A.A.; Elansary, H.O.; Farah, A.-H.H. Hydraulic Performance of Labyrinth-Channel Emitters: Experimental Study, ANN, and GEP Modeling. *Irrig. Sci.* **2020**, *38*, 1–16. [CrossRef]
35. Li, Y.; Feng, X.; Liu, Y.; Han, X.; Liu, H.; Sun, Y.; Li, H.; Xie, Y. Research on Hydraulic Properties and Energy Dissipation Mechanism of the Novel Water-Retaining Labyrinth Channel Emitters. *Agronomy* **2022**, *12*, 1708. [CrossRef]
36. Wang, C.; Li, Z.; Ma, J. Influence of Emitter Structure On its Hydraulic Performance Based On the Vortex. *Agriculture* **2021**, *11*, 508. [CrossRef]
37. Zhou, W.; Zhang, L.; Wu, P.; Cai, Y.; Zhao, X.; Yao, C. Hydraulic Performance and Parameter Optimisation of a Microporous Ceramic Emitter Using Computational Fluid Dynamics, Artificial Neural Network and Multi-Objective Genetic Algorithm. *Biosyst. Eng.* **2020**, *189*, 11–23. [CrossRef]
38. Falcucci, G.; Krastev, V.K.; Biscarini, C. Multi-Component Lattice Boltzmann Simulation of the Hydrodynamics in Drip Emitters. *J. Agric. Eng.* **2017**, *48*, 175–180. [CrossRef]
39. Huang, G. An Insight into Extreme Learning Machines: Random Neurons, Random Features and Kernels. *Cogn. Comput.* **2014**, *6*, 376–390. [CrossRef]
40. Zhang, G.; Li, Y.; Cui, D.; Mao, S.; Huang, G.-B. R-ELMNet: Regularized Extreme Learning Machine Network. *Neural Netw.* **2020**, *130*, 49–59. [CrossRef] [PubMed]
41. Solat, S.; Alinazari, F.; Maroufpoor, E.; Shiri, J.; Karimi, B. Modeling Moisture Bulb Distribution On Sloping Lands: Numerical and Regression-Based Approaches. *J. Hydrol.* **2021**, *601*, 126835. [CrossRef]
42. Maroufpoor, S.; Sammen, S.S.; Alansari, N.; Abba, S.; Malik, A.; Shahid, S.; Mokhtar, A.; Maroufpoor, E. A Novel Hybridized Neuro-Fuzzy Model with an Optimal Input Combination for Dissolved Oxygen Estimation. *Front. Environ. Sci.* **2022**, *10*, 1210. [CrossRef]
43. Behar, O.; Khellaf, A.; Mohammedi, K. Comparison of Solar Radiation Models and their Validation Under Algerian Climate—The Case of Direct Irradiance. *Energy Convers. Manag.* **2015**, *98*, 236–251. [CrossRef]
44. Saccone, D.; De Marchis, M.; Simos, T.E. Optimization of the Design of Labyrinth Emitter for Agriculture Irrigation Using Computational Fluid Dynamic Analysis. *AIP Conf. Proc.* **2018**, *2040*, 140013.
45. Li, S.; Yang, J.; Ansell, A. Discharge Prediction for Rectangular Sharp-Crested Weirs by Machine Learning Techniques. *Flow Meas. Instrum.* **2021**, *79*, 101931. [CrossRef]